Supporting Information

Dynamic Coordination Flexibility Unlocks Efficient Electrocatalytic Nitrate Reduction to Ammonia over Molecular Cobalt Catalysts

Zhongyang Yao[a]+, Kaiheng Zhao[b]+, Dayi Guo[c]+, Denglei Gao[d], Nobuhiro Hanada[a], Hideki Masuda[b], Menglei Yuan[e]*, Yaobing Wang[f]*, Zongjing Lu[a]**

Zhongyang Yao[a]+, Kaiheng Zhao[b]+, Dayi Guo[c]+, Denglei Gao[d], Nobuhiro Hanada[a], Hideki Masuda[b], Menglei Yuan[e]*, Zongjing Lu[a]*, Yaobing Wang[f]**

[a]Institute of Photochemistry and Photofunctional Materials, University of Shanghai for Science and Technology, Shanghai 200093, P. R. China

E-mail: zongjinglu@usst.edu.cn

[b] Key Laboratory of Photochemistry, Institute of Chemistry, Chinese Academy of Sciences Beijing 100190, P. R. China

[c] Institute of New Carbon-based Materials and Zero-carbon and Negative-carbon Technology, Lyuliang University, Lvliang 033001,Shanxi, P. R. China

[d] Shandong Key Laboratory of Green Electricity & Hydrogen Science and Technology, School of Chemical Engineering, Shandong Institute of Petroleum and Chemical Technology Dongying 257061, Shandong, P. R. China

E-mail: gaodenglei@sdipct.edu.cn

[e] State Key Laboratory of Solidification Processing and School of Materials Science and Engineering, Northwestern Polytechnical University, Xi'an 710072, Shaanxi, P. R. China

E-mail: mlyuan@nwpu.edu.cn

[f] CAS Key Laboratory of Design and Assembly of Functional Nano-structures, and Fujian Provincial Key Laboratory of Nanomaterials, State Key Laboratory of Structural Chemistry, Fujian Institute of Research on the Structure of Matter, Chinese Academy of Sciences

Fuzhou 350002, Fujian, P. R. China

E-mail: wangyb@fjirsm.ac.cn

†Zhongyang Yao, Kaiheng Zhao and Dayi Guo contributed equally to this paper.

*Corresponding author.

E-mail: zongjinglu@usst.edu.cn

^{1}H NMR spectroscopy

In order to verify the source of ammonia, $K^{15}NO_3$ was used as the raw nitrogen source to carry out the isotope labeled nitrate reduction experiment. 0.1 M PBS and 0.1 M $K^{15}NO_3$ were used as the electrolyte. After electroreduction, 2 mL of the obtained $^{15}NH_4^+$ electrolyte was taken out, and the pH value of the electrolyte was adjusted to weakly acidic with 1.0 M hydrochloric acid. Then 0.5 mL DMSO was added into 0.5 mL of the above mixed solution, and finally 1H NMR (600 MHz) was used for qualitative analysis.

In order to ascertain the production of NH_3, isotope labeling tracing experiments were conducted using a 100 mM $^{15}NO_3^-$ solution as the nitrogen source. To quantify the amount of generated NH_3, further analysis was carried out through proton nuclear magnetic resonance (1H NMR) spectroscopy. The specific procedure involved selecting malic acid as an internal standard. Subsequently, 100 μL of malic acid (3.2 mM), 300 μL of post-NO_3^- RR electrolyte, 100 μL of H_2SO_4 aqueous solution (4 M) and 100 μL of DMSO-d6 were thoroughly mixed. After adding tetramethylsilane, the mixture was transferred to an NMR tube, which was then sealed for the measurement using a nuclear magnetic resonance spectrometer to obtain the 1H NMR spectrum. Through the analysis of the integral areas of malic acid and the ammonium ethenyl singlet, the concentration of NH_3 was determined. Quantification of $NH_3$was performed by comparing the integrated area (I) of the olefinic singlet of maleic acid (δ = 6.25 ppm, 2H) with that of the characteristic ^{14}N–H triplet of ammonium (δ = 7.18 ppm, 4H, J = 52 Hz), according to the following equation:

$$c_{NH_4^+} = \frac{I_{NH_4^+}/H_{NH_4^+}}{I_s/H_s} \times c_s$$

where $c_{NH_4^+}$ and c_s are the concentration of ammonium and maleic acid (0.4 mg mL-1); $H_{NH_4^+}$ and H_s are the numbers of protons for ammonium and maleic acid; $I_{NH_4^+}$ and I_s are the integrals of ^{1}H NMR peaks for ammonium and maleic acid.

Differential Electrochemical Mass Spectrometry (DEMS) measurements.

For the DEMS measurement (Linglu Instruments QAS100), 0.1 M KOH electrolyte with 0.1 M KNO_3 was kept flowing into a specially designed electrochemical cell through a peristaltic pump. Ar was bubbled into the electrolyte constantly before and during the DEMS measurements. A carbon paper (1 × 1 cm²) loaded with Co-Dyn or Co-Rig was used as the working electrode, while Ag/AgCl and Pt wire electrodes served as the reference and counter electrodes, respectively. Linear sweep voltammetry technology was employed from 0 to –0.6 V versus RHE at a scan rate of 5 mV s^{-1} until the baseline kept steady. Then, the corresponding mass signals appeared. After the electrochemical test was over and the mass signal returned to baseline, the next cycle was started. After five cycles, the experiment was ended.

Electrochemical in situ FTIR tests

In situ FTIR spectra were collected using a Thermo Fisher iS50 FTIR spectrometer. The working electrode was prepared by plating a monocrystalline silicon wafer with a thin layer of gold to enhance the surface signal. To prepare the catalyst ink, 2.0 mg of Co-Dyn or Co-Rig catalyst and 10 μL of Nafion solution were dispersed in 100 μL of ethanol and ultrasonicated for 1 hour to obtain a homogeneous suspension. Then, 100 μL of the ink was

carefully drop-cast onto the gold-coated silicon substrate and used as the working electrode. A platinum foil and an Ag/AgCl electrode served as the counter and reference electrodes, respectively. The electrolyte consisted of 1 M KOH with 0.1 M KNO_3. Prior to measurement, the background spectrum of the working electrode was recorded under open-circuit potential. Constant potential electrolysis was tested from open circuit potential (OCP) to -1.0 V at 200 mV intervals.

Computational Details

All first-principles calculations within this study were performed employing spin-polarized density functional theory (DFT) as implemented in the Vienna ab initio simulation package (VASP)[1]. The generalized gradient approximation (GGA) parameterized by the Perdew–Burke–Ernzerhof (PBE) functional was adopted to treat exchange–correlation effects[2, 3]. Electron–ion interactions were modeled using the projector augmented wave (PAW) approach.[4]4 A plane-wave basis set with a kinetic energy cutoff of 500 eV was applied in all simulations. Geometry optimizations were considered converged when the energy change between successive steps fell below 10^{-5} eV and the residual forces on atoms were less than 0.02 eV/Å. For Brillouin zone integration, a 3 × 3 × 1 Monkhorst–Pack k-point mesh was used during structural relaxations, whereas a finer 6 × 6 × 1 grid was employed for evaluating electronic properties[5]. To properly account for van der Waals interactions, the DFT-D3 dispersion correction scheme by Grimme was incorporated[6].

The Gibbs free energy change (ΔG) associated with each hydrogenation step was computed within the framework of the computational hydrogen electrode (CHE) model[7], expressed as: $\Delta G = \Delta E + \Delta E_{ZPE} - T\Delta S + \Delta G_U + \Delta G_{pH}$. Here, ΔE corresponds to the total energy difference obtained from DFT, ΔE_{ZPE} represents the zero-point energy correction, and $T\Delta S$ accounts for entropy effects at 298.15 K and 0.1 MPa. Vibrational frequency analyses were employed to extract ZPE and entropy values for adsorbed intermediates. The entropies of the free molecules (NO, H_2, N_2O, and NH_3) are obtained from the NIST database (https://doi.org/10.18434/T4D303). The effect of electrode potential is included via the ΔG_U term, while the influence of solution pH is incorporated as $\Delta G\text{pH} = k_B T \times \ln 10 \times \text{pH}$, with pH set to zero. The theoretical limiting potential (U_L) was estimated from $U_L = -\Delta G_{max}/e$, where ΔG_{max} denotes the maximum free energy change along the reaction pathway.

To avoid directly computing the energy of charged NO_3^-, gaseous HNO_3 is used as a reference in the following steps[8, 9].

$$HNO_3(g) \rightarrow HNO_3(l)$$
$$HNO_3(l) \rightarrow H^+ + NO_3^-$$
$$* + NO_3^- \rightarrow {}^*NO_3 + e^-$$

As a result, the NO_3^- adsorption can be described as

$* + HNO_3(g) \rightarrow {}^*NO_3 + H^+ + e^-$

Correspondingly, the adsorption energy of NO_3^-[$\Delta G(*NO_3)$] can be approximately expressed as

$$\Delta G(*NO_3) = G(*NO_3) - G(*) - G(HNO_3(g)) + 0.5G(H_2(g)) + \Delta G(\text{correct})$$
$$\Delta G(\text{correct}) = -\Delta G(S1) - \Delta G(S2)$$

where $G(*NO_3)$, $G(*)$, $G(HNO_3(g))$, and $0.5G(H_2(g))$ are the Gibbs free energy of NO_3^- adsorbed on Co-based SACs, Co-based SACs, HNO3 and H2 molecules in the gas phase, respectively. ΔG(correct) denotes the correction of adsorption energy. According to CRC handbook of chemistry and physics[10], $\Delta G(S1)$ = -0.075 eV and $\Delta G(S2)$ = -0.317 eV. Therefore, ΔG(correct) is set to 0.075 + 0.317 = 0.392 eV.

The elementary steps of NO_3RR pathway

The electrochemical reduction of NO_3^- to NH_3 involves the transfer of nine protons and eight electrons. All the reactions can be summarized as follows:

$NO_3^- + 9H^+ + 8e^- \rightarrow NH_3 + 3H_2O$

Involving the intermediates $^*NO_3$, $^*NO_2$, $^*NO$, $^*NOH$, $^*N$, $^*NH$, $^*NH_2$ and $^*NH_3$, the NO_3RR on designed catalysts surfaces were simulated according to the following reactions:

$$^* + NO_3^- \rightarrow {}^*NO_3 + e^-$$

$$^*NO_3 + H_2O + 2e^- \rightarrow {}^*NO_2 + 2OH^-$$

$$^*NO_2 + H_2O + 2e^- \rightarrow {}^*NO + 2OH^-$$

$$^*NO + H_2O + e^- \rightarrow {}^*NOH + 2OH^-$$

$$^*NOH + e^- \rightarrow {}^*N + OH^-$$

$$^*N + H_2O + e^- \rightarrow {}^*NH + OH^-$$

$$^*NH + H_2O + e^- \rightarrow {}^*NH_2 + OH^-$$

$$^*NH_2 + H_2O + e^- \rightarrow {}^*NH_3 + OH^-$$

$$^*NH_3 \rightarrow {}^* + NH_3$$

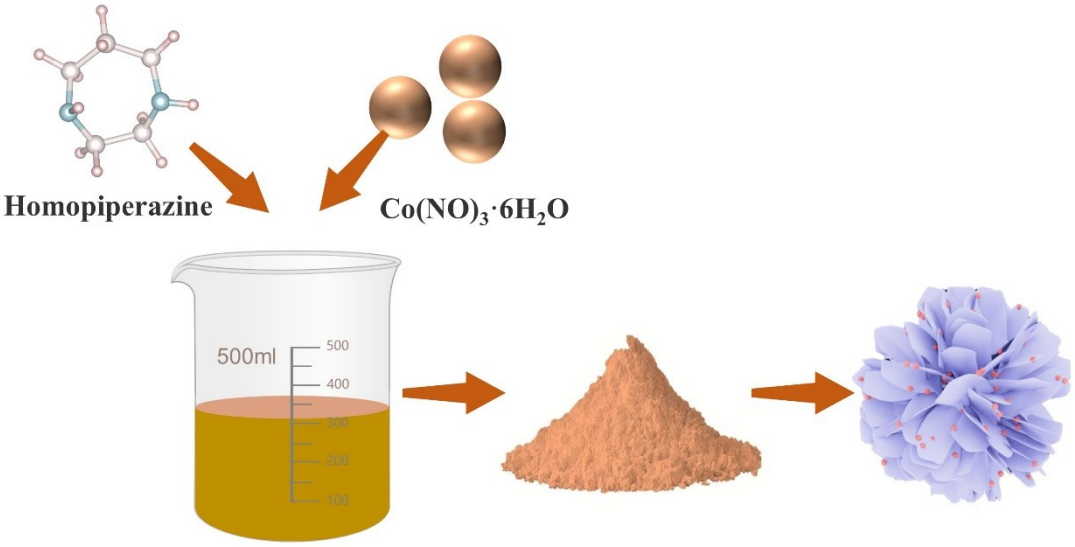

Figure S1. Schematic diagram for the synthesis of Co-Dyn catalysis.

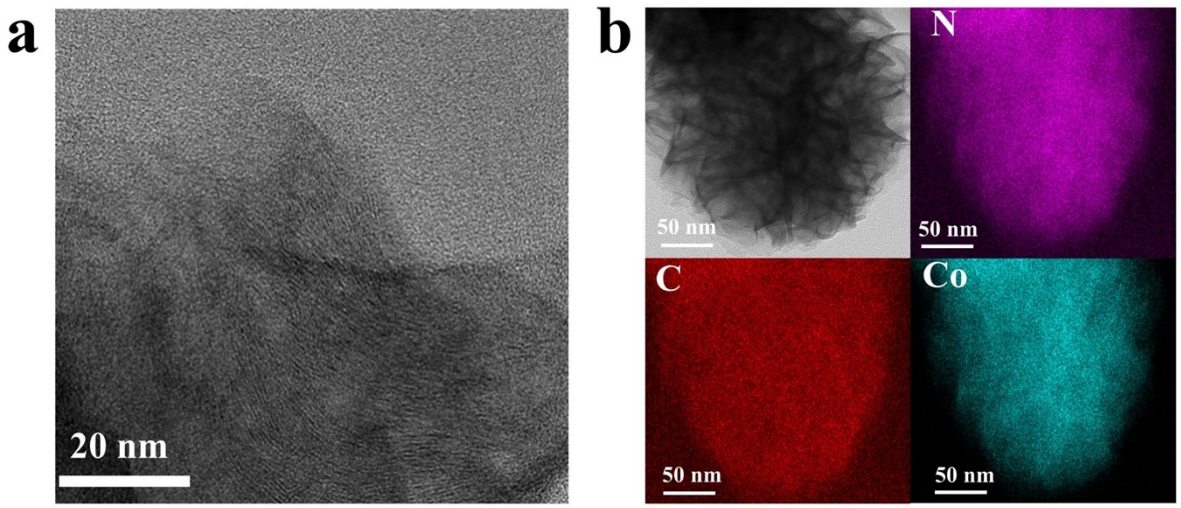

Figure S2. a) High-resolution TEM, b) HAADF-TEM and corresponding elemental mapping images of Co-Dyn.

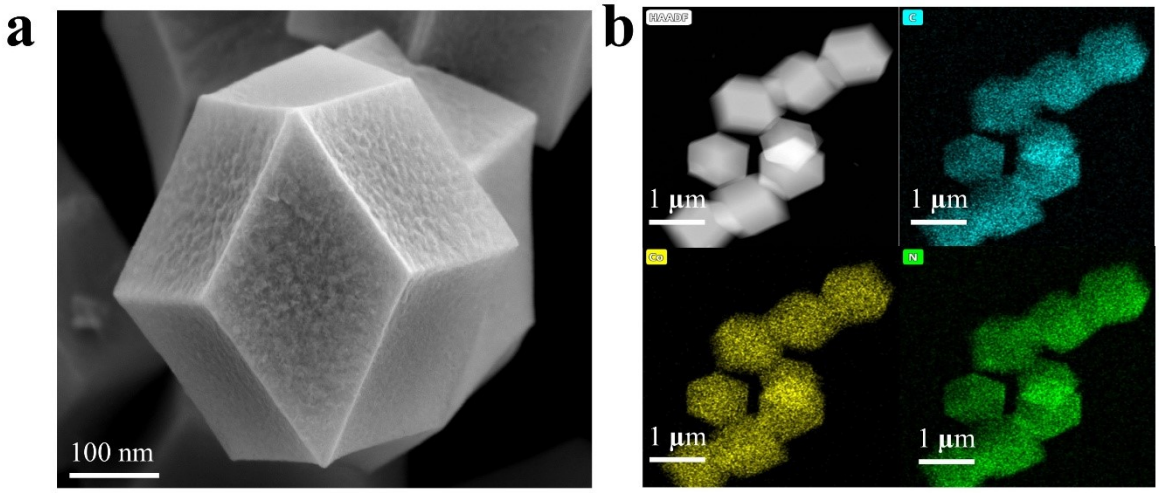

Figure S3. a) SEM, b) HAADF-TEM and corresponding elemental mapping images of Co-Rig.

100 nm

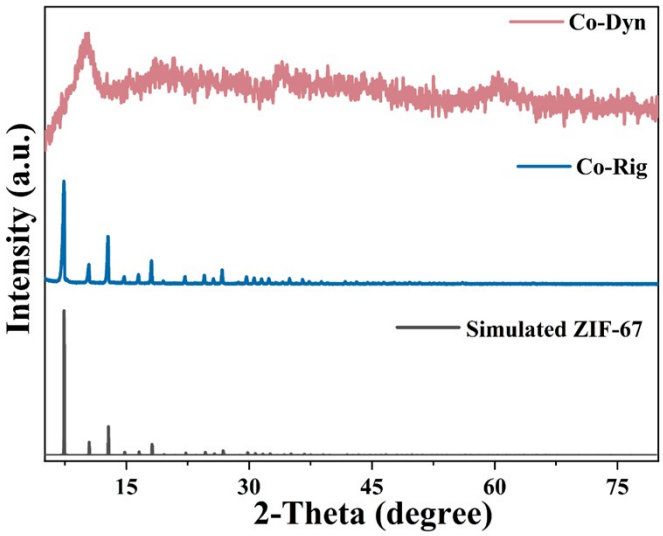

Figure S4. XRD patterns of Co-Dyn and Co-Rig.

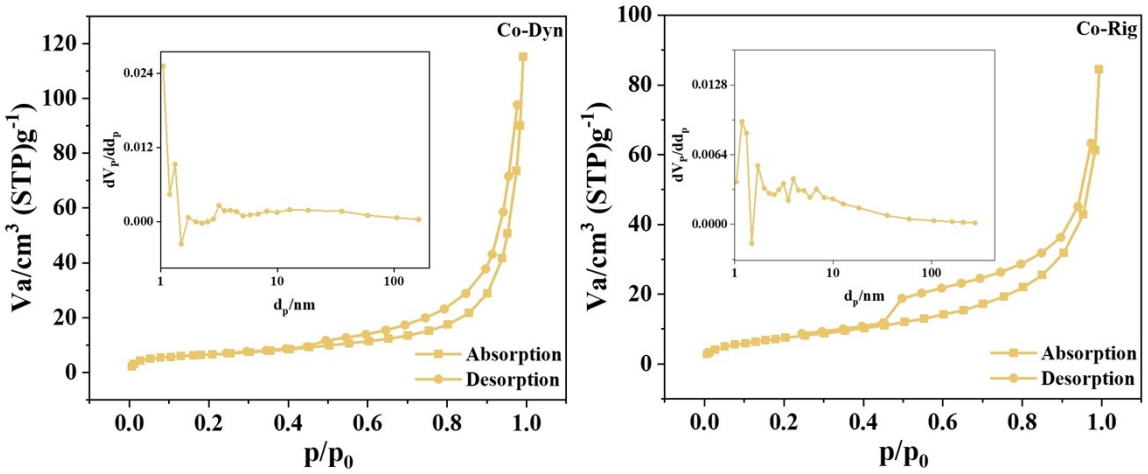

Figure S5. N_2 adsorption/desorption isotherms of Co-Rig and Co-Dyn, the inset is the corresponding pore size distribution.

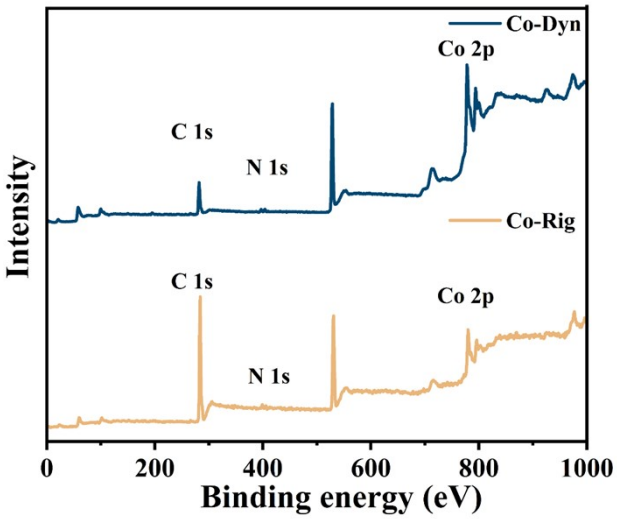

Figure S6. XPS survey spectra of Co-Dyn and Co-Rig.

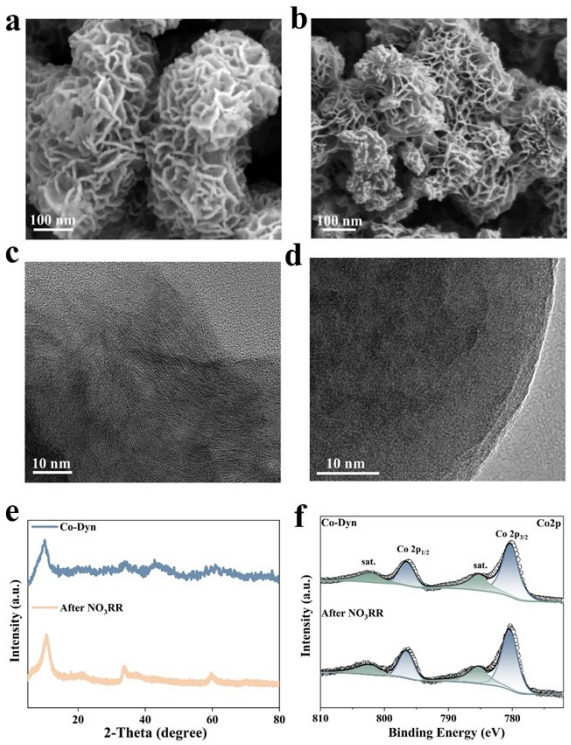

Figure S7. Structural and compositional stability of Co-Dyn before and after NO_3RR. (a, b) SEM images of Co-Dyn before (a) and after (b) NO_3RR. (c, d) High-resolution TEM images of Co-Dyn before (c) and after (d) NO_3RR (e) XRD patterns of Co-Dyn before and after NO_3RR.(f) High-resolution Co and N XPS spectra of Co-Dyn before and after NO_3RR.

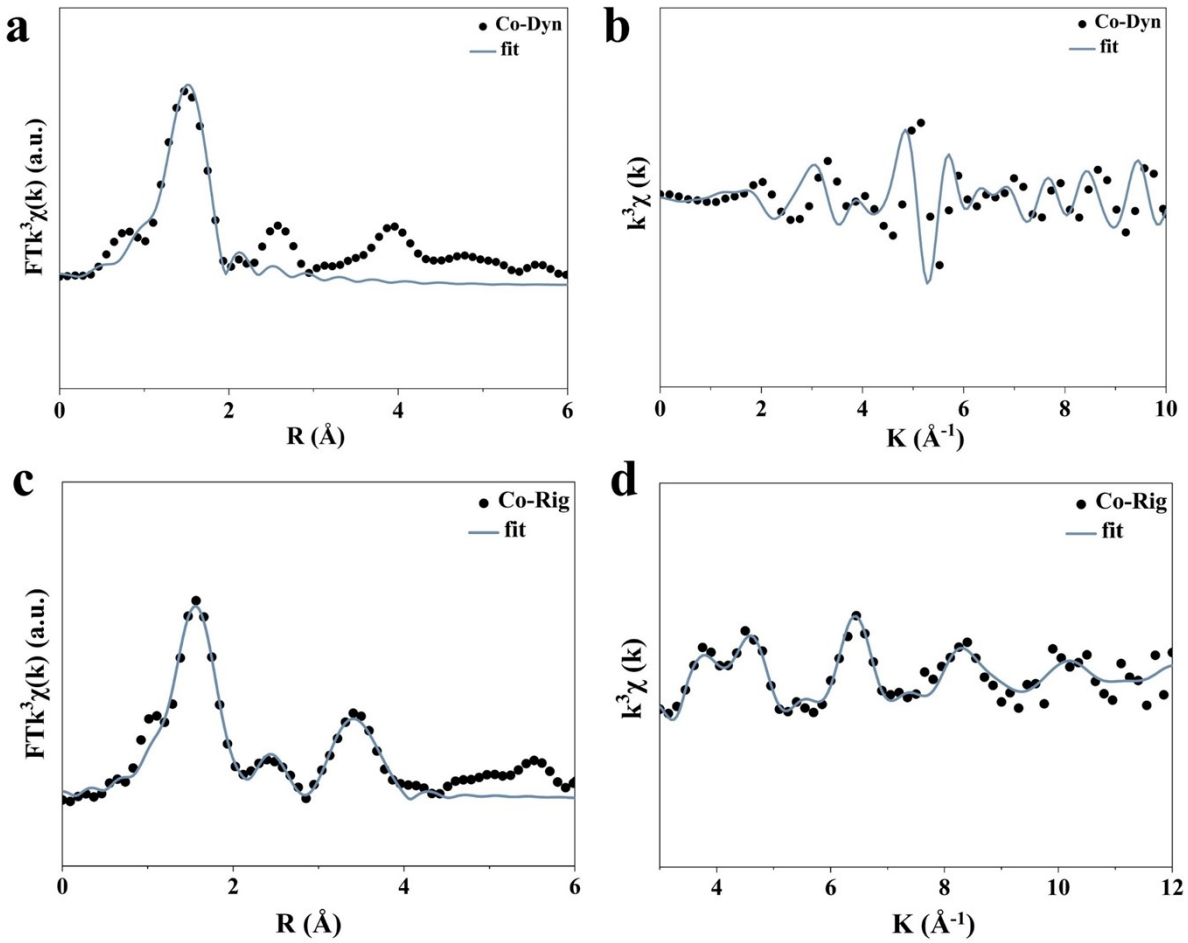

Figure S8. (a, b) k^3-weighted EXAFS oscillation curves ($k^3\chi(k)$) and corresponding fitting results for Co-Dyn and Co-Rig. c, d) Magnitude of the Fourier-transformed EXAFS spectra (FT($k^3\chi(k)$)) and fitting results.

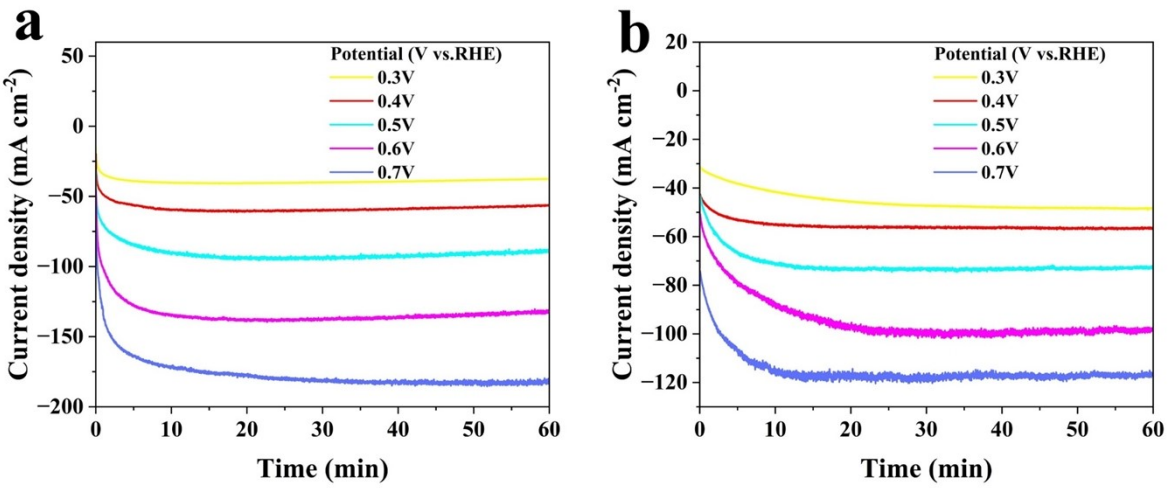

Figure S9. Time-dependent current density curves of a) Co-Dyn and b) Co-Rig for the NO_3RR at different potentials in 1 M KOH with 0.1 M NO_3^-.

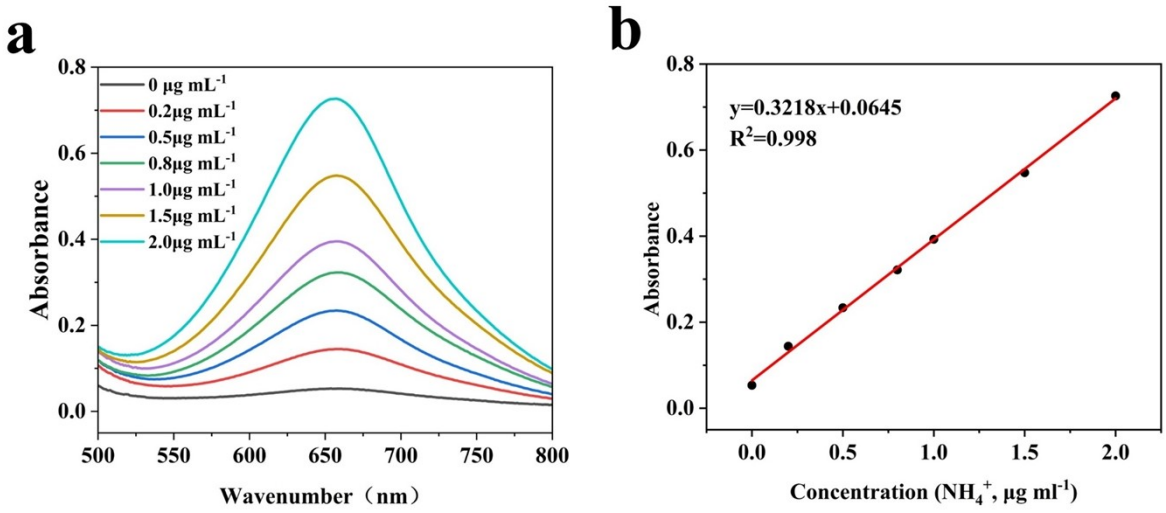

Figure S10. a) UV-vis spectra of NH_4Cl solutions with known concentrations and b) linear fitting results of the calibration curve.

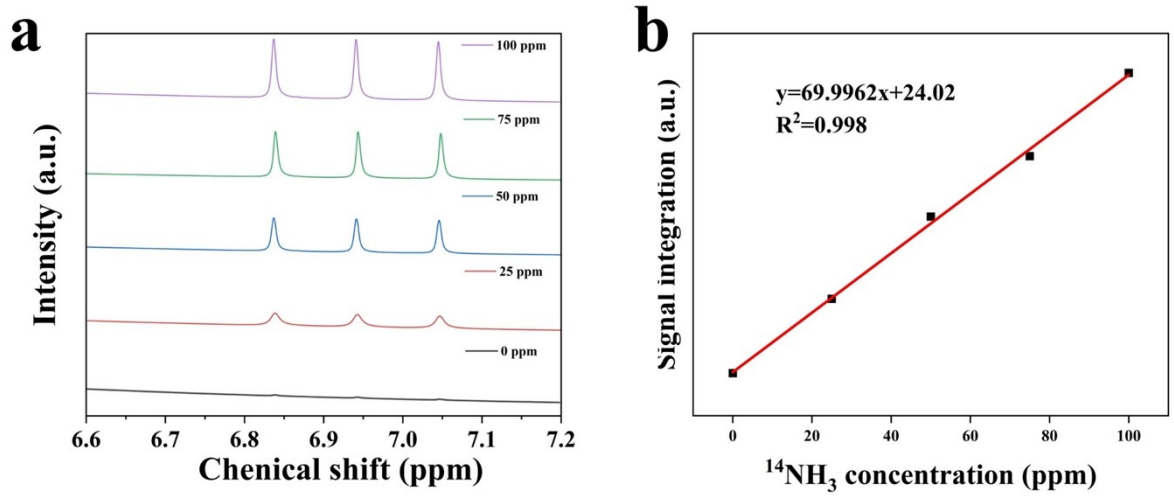

Figure S11. a) ^{1}H NMR spectra of NH_4^+ at different known concentrations and b) linear fitting results of the calibration curve.

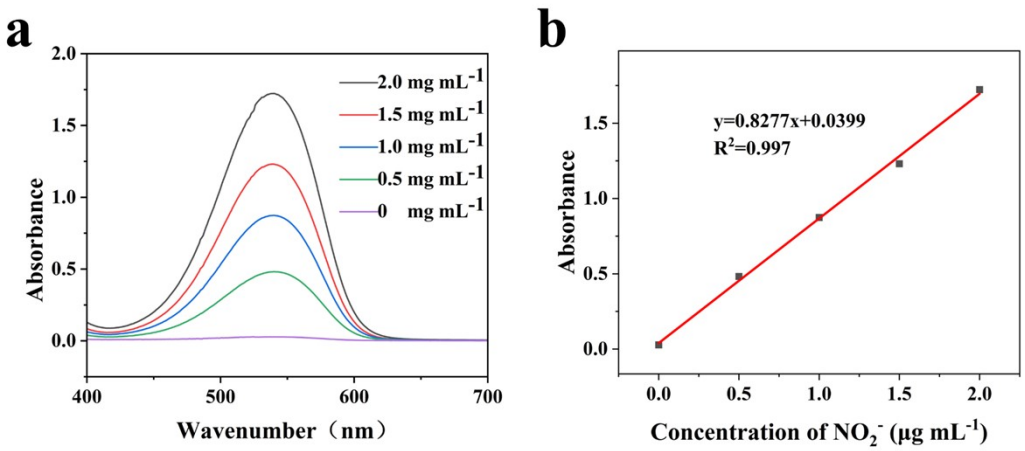

Figure S12. a) UV–vis spectra of NO_2^- standard solutions with different concentrations and b) linear fitting results of the corresponding calibration curve.

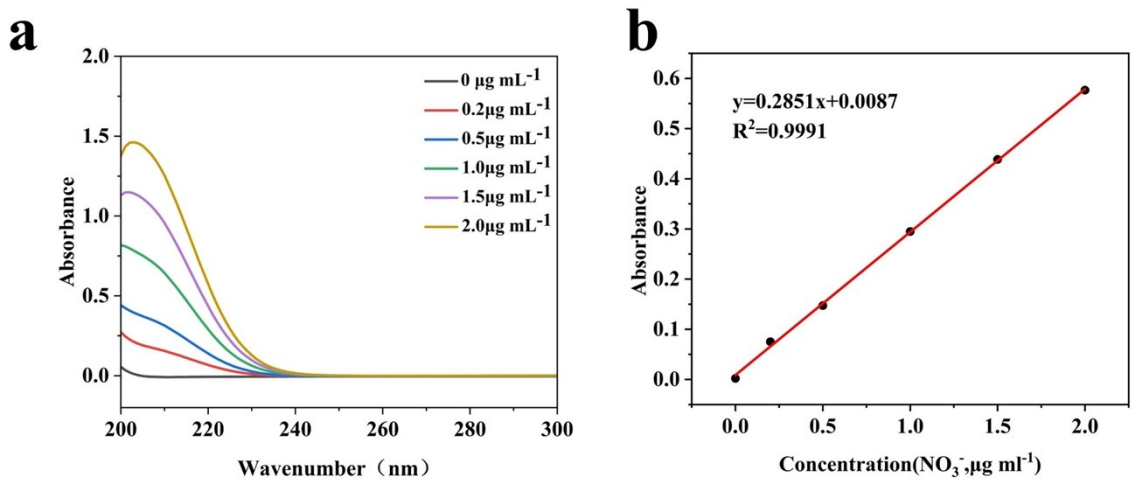

Figure S13. a) UV–vis spectra of NO_3^- standard solutions with different concentrations and b) linear fitting results of the corresponding calibration curve.

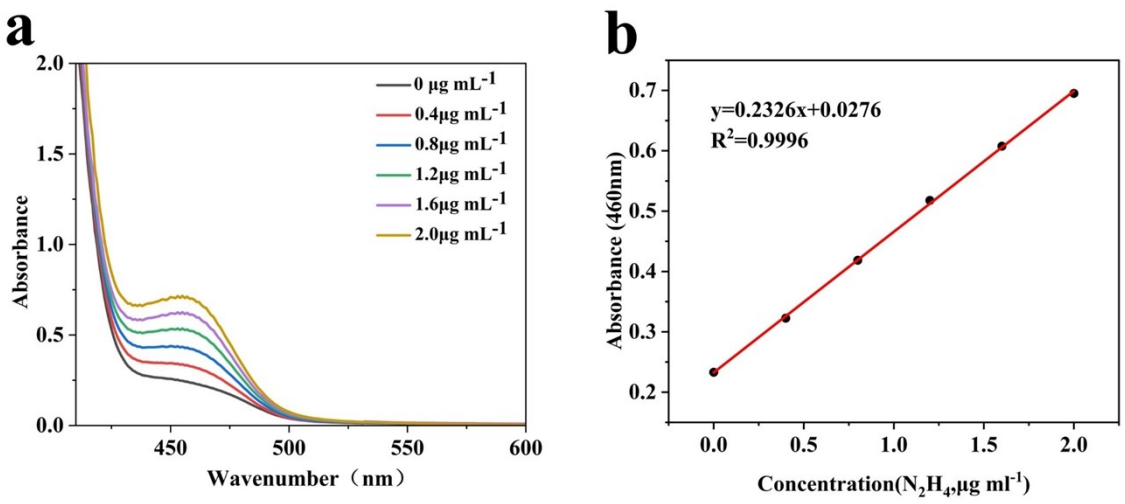

Figure S14. a) UV–vis spectra of N_2H_4 standard solutions with different concentrations and b) linear fitting results of the corresponding calibration curve.

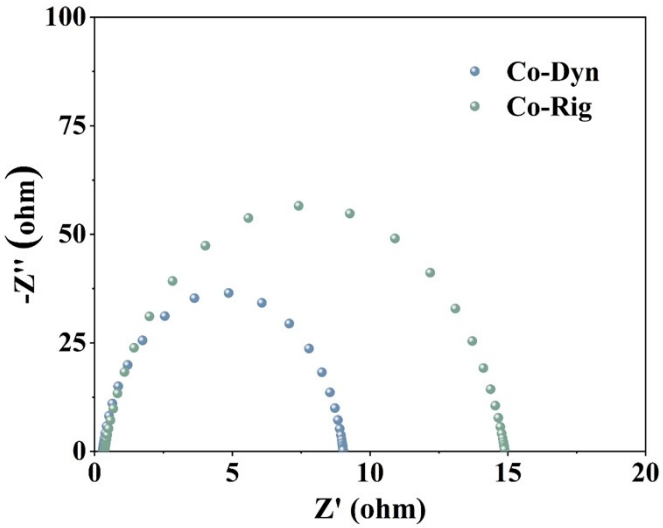

Figure S15. EIS spectra of Co-Dyn and Co-Rig.

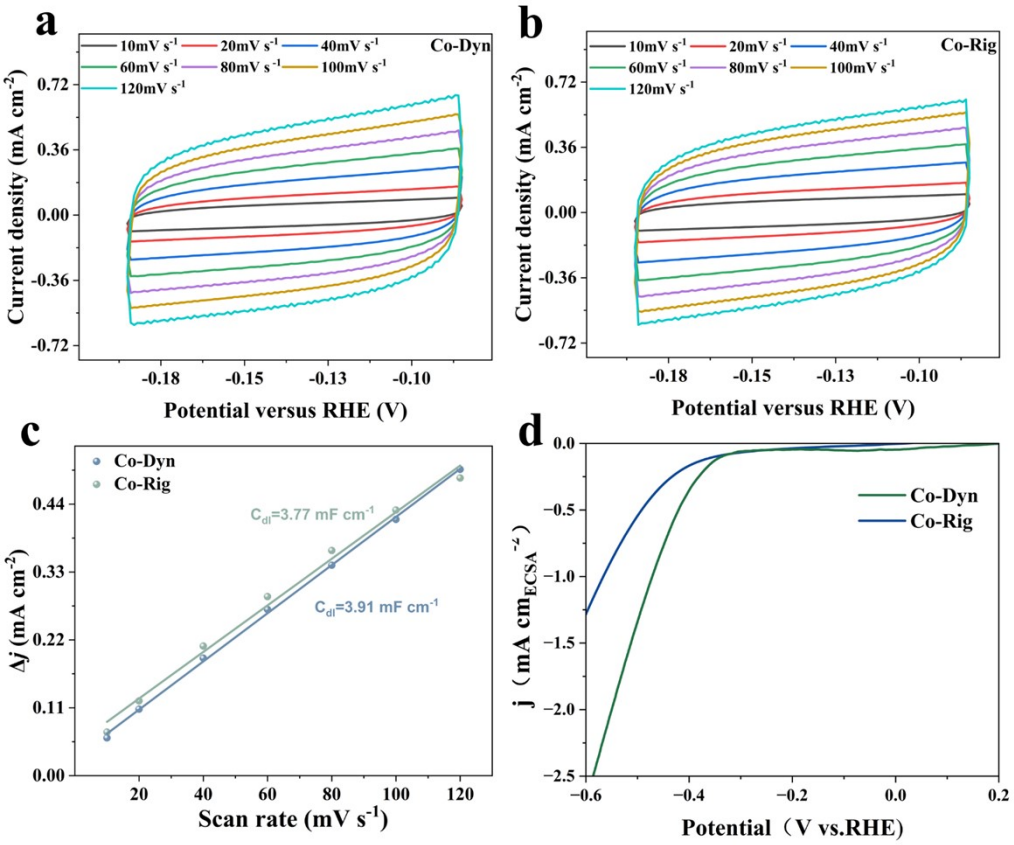

Figure S16. (a,b) Cyclic voltammograms of Co-Dyn (a) and Co-Rig (b) recorded in a non-faradaic potential window at different scan rates. (c) Capacitive current density (Δj = (janodic − jcathodic)/2 at 0.14 V vs. RHE) plotted as a function of scan rate for Co-Dyn and Co-Rig, used to extract the double-layer capacitance (Cdl). The fitted slopes give Cdl values of 3.91 and 3.77 mF cm^{-2} for Co-Dyn and Co-Rig, respectively, indicating similar electrochemically active surface areas (ECSAs). (d) NO3RR polarization curves of Co-Dyn and Co-Rig normalized by ECSA, showing that Co-Dyn retains substantially higher intrinsic activity than Co-Rig over the entire potential range.

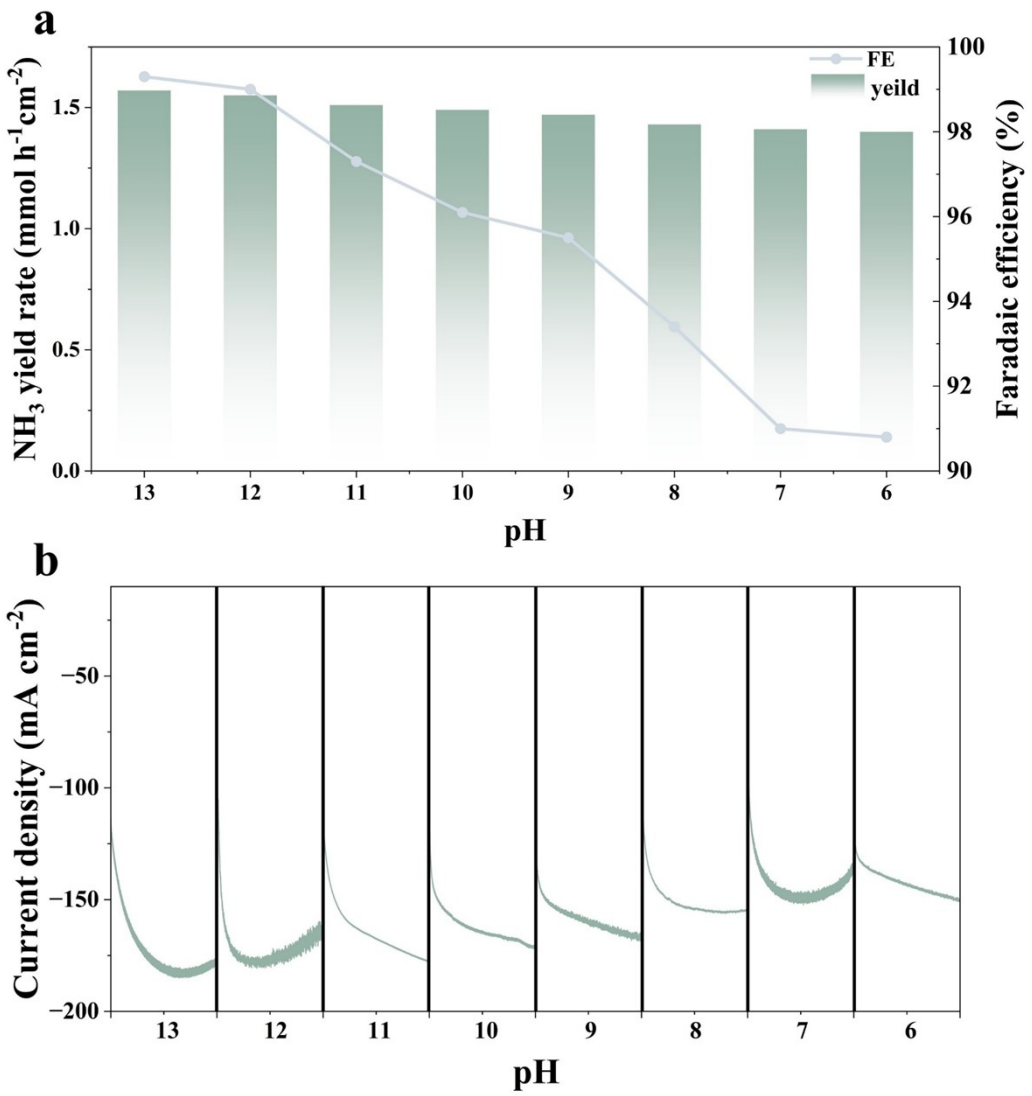

Figure S17. (a) NH_3 yield rate and Faradaic efficiency (FE) of Co-Dyn for NO_3RR at different pH values (6–13) at –0.70 V vs. RHE. (b) Corresponding chronoamperometric i–t curves recorded at –0.70 V vs. RHE for Co-Dyn in electrolytes with different pH values, showing stable current densities over 1 h.

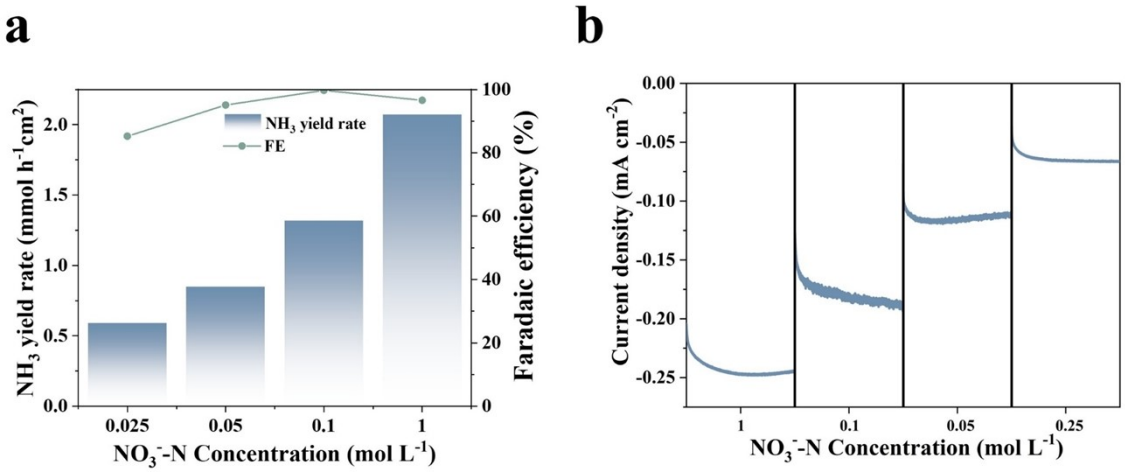

Figure S18. (a) NH_3 yield rate and Faradaic efficiency (FE) of Co-Dyn for NO_3RR at different NO_3^-–N concentrations (0.025–1.0 M) at –0.70 V vs. RHE. (b) Corresponding chronoamperometric i–t curves recorded at –0.70 V vs. RHE for Co-Dyn in electrolytes with different NO_3^-–N concentrations, demonstrating concentration-dependent current densities with good temporal stability.

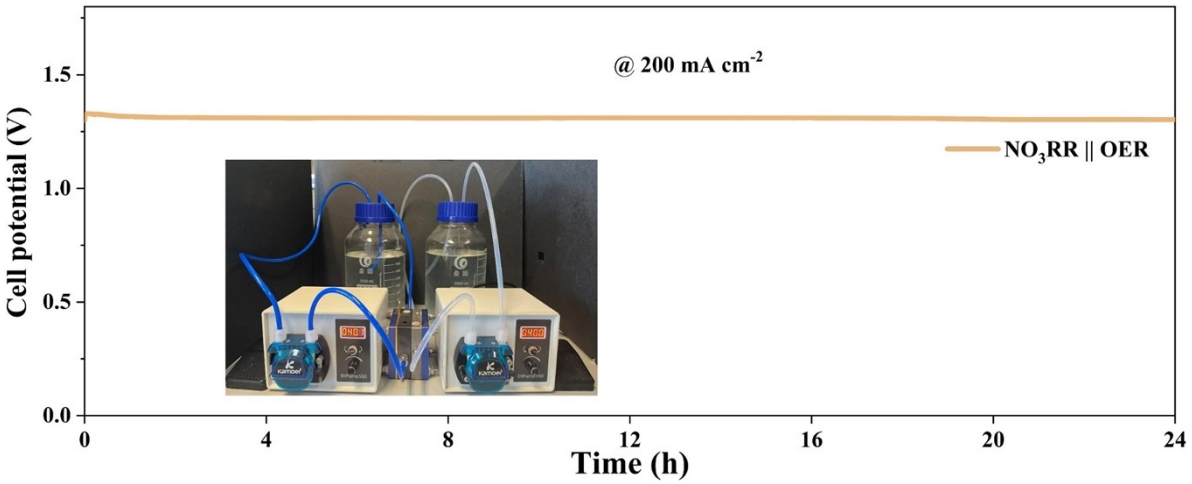

Figure S19. Stability of the Co-Dyn electrode in the MEA at 200 mA cm^{-2} (with iR compensation). The electrolyte is a mixed solution of 1.0 M KOH + 0.1 M KNO_3.

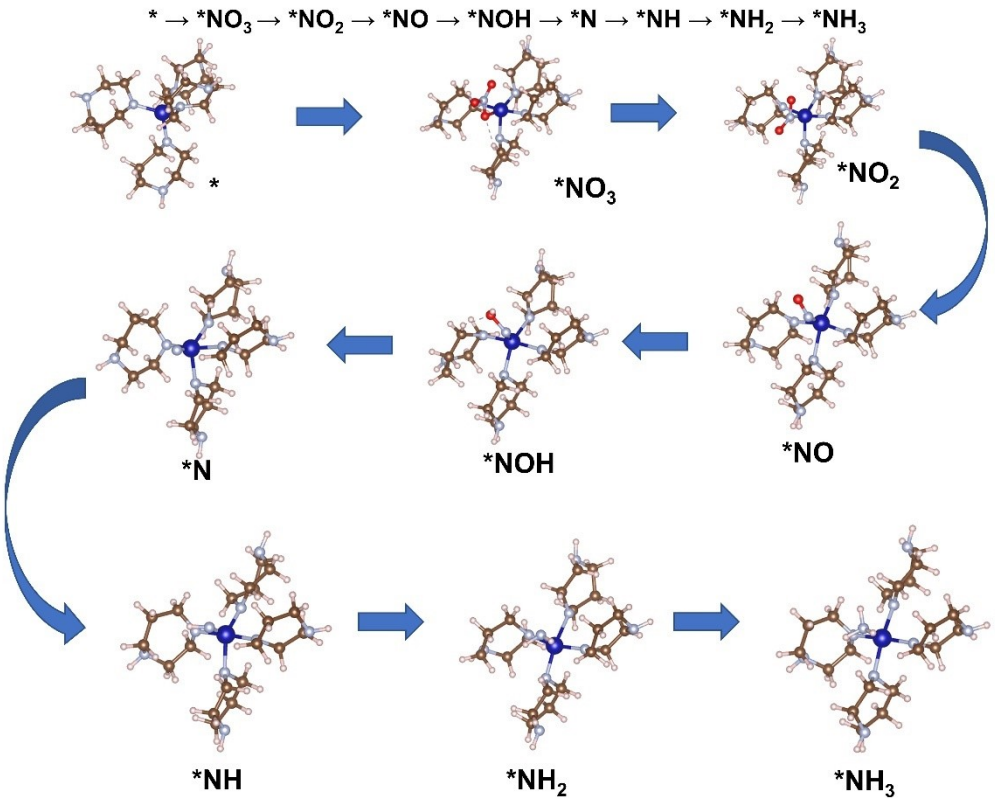

Figure S20. The adsorption configuration diagrams of reactants, intermediates, and products involved in the NO_3RR on Co-Dyn.

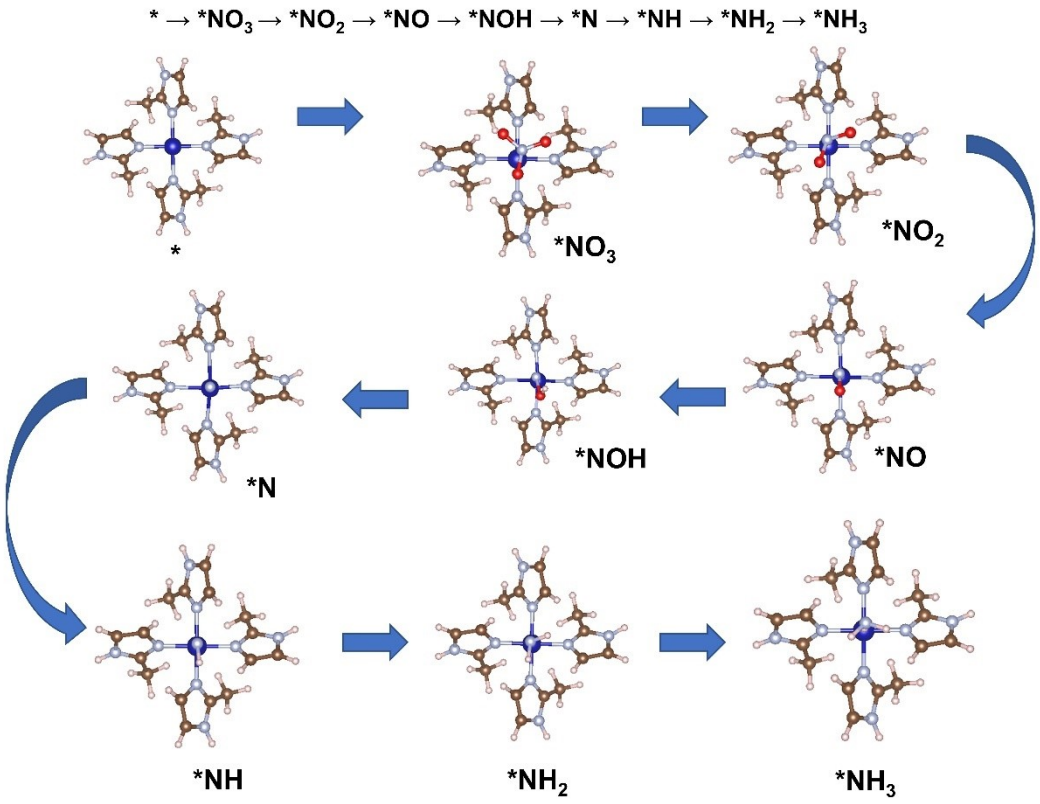

Figure S21. The adsorption configuration diagrams of reactants, intermediates, and products involved in the NO_3RR on Co-Rig.

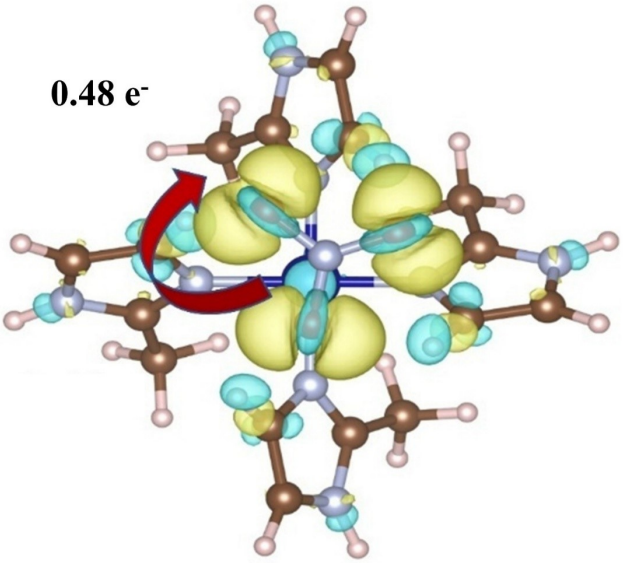

Figure S22. difference Charge density between *NO_3 and Co-Rig.

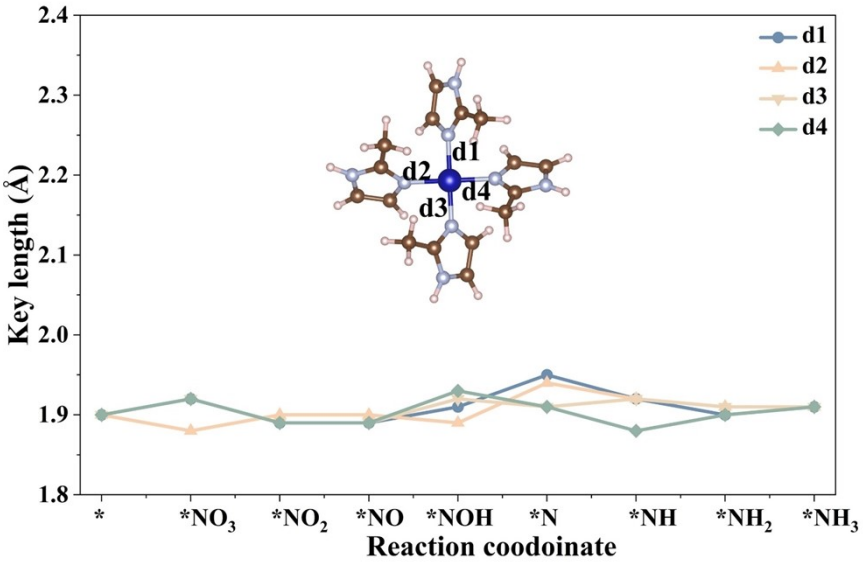

Figure S23. Statistics of the in-plane Co-N coordination bond lengths of Co-Rig in the most favorable pathway of the NO_3RR.

Table S1. Bulk and surface Co contents of Co-Dyn before and after NO_3RR determined by ICP, XPS analyses.

Sample	At.%	Wt.%
XPS	4.1	16.1
XPS after NO_3RR	4.0	15.9
ICP	4.2	16.3
ICP after NO_3RR	4.1	16.2

Table S2. EXAFS fitting parameters of Co-Dyn and Co-Rig at the Co K-edge.

Sample	Path	CN	R (Å)	σ^2 (10^{-3}Å^2)	ΔE_0 (eV)	R-factor
Co-Rig	Co-N	4.0	1.92 ± 0.02	7.5 ± 0.3	1.5 ± 0.3	0.010
Co-Dyn	Co-N	4.0	1.93 ± 0.02	8.0 ± 0.6	0.8 ± 0.4	0.012
Co foil	Co-Co	12.0	2.50 ± 0.01	7.7 ± 0.3	2.0 ± 0.5	0.008

CN represents the coordination number, **R** denotes the average bond distance to the neighboring atom, **σ^2** corresponds to the mean square relative displacement (MSRD), and **ΔE_0** refers to the inner potential correction. The fitting quality is evaluated by the **R factor**, which reflects the degree of agreement between experimental and simulated spectra. The amplitude reduction factor (**S_0^2**) was fixed at 0.87, determined from the reference fit of Co foil with its crystallographic coordination number (marked with the symbol *). The obtained parameters all fall within a reasonable range for reliable EXAFS fitting: $0.700 < S_0^2 < 1.000$, CN > 0, $\sigma^2 > 0.002$ Å^2, $|\Delta E_0| <$ 15 eV, and R factor < 0.02.

Table S3. Summary of electrocatalytic nitrate reduction performance for state-of-the-art catalysts reported in recent literature.

Catalysts	Electrolyte	NH_3 yield	FE (%)	Reference
Cu-CoO/$Co(OH)_2$	1.0 M KOH + 0.1 M NO_3^-	0.43 mmol h^{-1} cm^{-2}	94.7	[11]
Co-NCNT	0.1 M NaOH + 0.1 M NO_3^-	0.35 mmol h^{-1} cm^{-2}	92.0	[12]
R-Co/CF	1.0 M KOH + 0.1 M NO_3^-	0.87 mmol h^{-1} cm^{-2}	96.2	[13]
$(Cu_{0.6}Co_{0.4})Co_2O_4$	1.0 M KOH + 0.1 M NO_3^-	1.09 mmol h^{-1} cm^{-2}	96.5	[14]
SN Co Li+/PCNF	0.5 M Na_2SO_4 + 0.5 M KNO_3	0.75 mmol h^{-1} cm^{-2}	72.7	[15]
Co SACs	0.02 M Na_2SO_4 + 100 ppm NO_3^-	0.02 mmol h^{-1} cm^{-2}	92	[16]
Fe_2Co MOF	0.05 M H_2SO_4+0.05M NO_3^-	0.17 mmol h^{-1} cm^{-2}	86.5	[17]
$Cu/Co_{0.85}Se_{VSe}$	1 M KOH+0.1 M NO_3^-	0.14 mmol h^{-1} cm^{-2}	93.5	[18]
Co-P/NPG	0.5 M K_2SO_4+0.1 M NO_3^-	0.50 mmol h^{-1} cm^{-2}	93.8	[19]
Co+Bi@Cu NW	0.1 M Na_2SO_4+0.05 M NO_3^-	0.11 mmol h^{-1} cm^{-2}	99.5	[20]
$Ag–Co_3O_4$	0.1 M OH^- + 0.1 M NO_3^-	0.052 mmol h-1 cm^{-2}	88	[21]
Co–P–O/C	0.1 M OH^- + 0.1 M NO_3^-	0.402 mmol h^{-1} cm^{-2}	97	[22]
CoP/TiO_2@TP	0.1 M OH^- + 0.1 M NO_3^-	0.4998 mmol h^{-1} cm^{-2}	95	[23]
CuCo-TPA-E	1 M KOH 0.1 M KNO_3	1.12 mmol h^{-1} cm^{-2}	99	[24]
CoFe LDH	1 M KOH (1400 ppm NO_3^-)	0.93 mmol h^{-1} cm^{-2}	97.68	[25]
Co-Dyn	1 M KOH 0.1 M KNO_3	1.56 mmol h^{-1} cm^{-2}	99.98	**This work**

Supporting References

1. G. Kresse and J. Hafner, Physical Review B, 1993, 47, 558-561.
2. J. P. Perdew, J. A. Chevary, S. H. Vosko, K. A. Jackson, M. R. Pederson, D. J. Singh and C. Fiolhais, Physical Review B, 1992, 46, 6671-6687.
3. J. P. Perdew and Y. Wang, Physical Review B, 1992, 45, 13244-13249.
4. G. Kresse and D. Joubert, Phys. Rev. B., 1999, 59, 1758-1775.
5. H. J. Monkhorst and J. D. Pack, Physical Review B, 1976, 13, 5188-5192.
6. S. Grimme, J. Antony, S. Ehrlich and H. Krieg, J Chem Phys, 2010, 132, 154104.
7. J. Norskov, J. Rossmeisl, A. Logadottir, L. Lindqvist, J. Kitchin, T. Bligaard and H. Jónsson, J. Phys. Chem. B, 2004, 108, 17886-17892.
8. S. Guo, K. Heck, S. Kasiraju, H. Qian, Z. Zhao, L. C. Grabow, J. T. Miller and M. S. Wong, ACS catalysis, 2017, 8.
9. J.-X. Liu, D. Richards, N. Singh and B. R. Goldsmith, ACS Catalysis, 2019, 9, 7052-7064.
10. R. C. Weast, *CRC handbook of chemistry and physics*, CRC Press, Boca Raton, FL, 1988.
11. Y. Zhang, T. Gao, F. Zhang, X. Qu, Y. Luo, P. Zhang, J. Liang, Y. Song, F. Fang, F. Wang, D. Sun and Y. Liu, Advanced Energy Materials, 2024, 14.
12. J. Chen, Q. Zhou, L. Yue, D. Zhao, L. Zhang, Y. Luo, Q. Liu, N. Li, A. A. Alshehri, M. S. Hamdy, F. Gong and X. Sun, Chemical Communications, 2022, 58, 3787-3790.
13. H. Wang, B. Yang, R. L. Smith, Y. Su and X. Qi, Advanced Functional Materials, 2025, 35.
14. X.-C. Li, T.-T. Huang, Y. Hu, X. Li, Y.-F. Liu, H. Dong, C.-J. Jia, G.-S. Li and Y.-W. Zhang, Applied Catalysis B: Environment and Energy, 2025, 366.
15. L. Sun, C. Dai, T. Wang, X. Jin, Z. J. Xu and X. Wang, Angewandte Chemie International Edition, 2024, 63.
16. Proceedings of the National Academy of Sciences, https://doi.org/10.1073/pnas.
17. Y. Lv, S. W. Ke, Y. Gu, B. Tian, L. Tang, P. Ran, Y. Zhao, J. Ma, J. L. Zuo and M. Ding, Angewandte Chemie International Edition, 2023, 62.
18. Z. Gu, Y. Zhang, X. Wei, Z. Duan, Q. Gong and K. Luo, Advanced Materials, 2023, 35.
19. J. Ni, J. Yan, F. Li, H. Qi, Q. Xu, C. Su, L. Sun, H. Sun, J. Ding and B. Liu, Advanced Energy Materials, 2024, 14.
20. R. Zhao, Q. Yan, L. Yu, T. Yan, X. Zhu, Z. Zhao, L. Liu and J. Xi, Advanced Materials, 2023, 35.
21. M. Zhang, Z. Ma, S. Zhou, C. Han, V. Kundi, P. V. Kumar, L. Thomsen, B. Johannessen, L. Peng, Y. Shan, C. Tsounis, Y. Yang, J. Pan and R. Amal, ACS Catalysis, 2024, 14, 11231-11242.
22. F. Lei, M. Xu, Y. Zhang, J. Yu, M. Zhang, R. Huai, J. Xie, P. Hao, G. Cui and B. Tang, Journal of Materials Chemistry A, 2023, 11, 16854-16859.
23. Z. Deng, C. Ma, X. Fan, Z. Li, Y. Luo, S. Sun, D. Zheng, Q. Liu, J. Du, Q. Lu, B. Zheng and X. Sun, Materials Today Physics, 2022, 28.
24. J. Yang, W.-D. Zhang, H. Zhao, Y. Zou, Z.-Y. Zhang, J. Liu, J. Wang, Z.-G. Gu and X. Yan, Applied Catalysis B: Environmental, 2024, 340.
25. F. Du, J. Li, C. Wang, J. Yao, Z. Tan, Z. Yao, C. Li and C. Guo, Chemical Engineering Journal, 2022, 434.